Chemical Engineering Journal 157 (2010) 379–392

Contents lists available at ScienceDirect

Chemical Engineering Journal

journal homepage: www.elsevier.com/locate/cej

Characterization of fluid dynamics and mass-transfer in an electrochemical oxidation cell by experimental and CFD studies

J.L.C. Santos[a,*], V. Geraldes[b], S. Velizarov[a], J.G. Crespo[a]

[a] REQUIMTE/CQFB, Department of Chemistry, Faculdade de Ciências e Tecnologia, Universidade Nova de Lisboa, 2829-516 Caparica, Portugal
[b] Department of Chemical and Biological Engineering, Instituto Superior Técnico, Universidade Técnica de Lisboa, Av. Rovisco Pais 1, 1049-001 Lisbon, Portugal

ARTICLE INFO

Article history:
Received 10 July 2009
Received in revised form
16 November 2009
Accepted 17 November 2009

Keywords:
Computational fluid dynamics (CFD)
Borod-doped diamond anode
Limiting current technique
Mass-transfer correlations
DiaCell
Electrochemical oxidation

ABSTRACT

Flow and mass-transfer in a widely used commercial electrochemical flow cell (DiaCell®) were investigated by computational fluid dynamics (CFD) simulations and validated by experimental measurements. Both qualitative and quantitative comparisons were made for distinct flow regimes in the Reynolds range between 25 and 2500 (based on the inter-electrode distance and on the superficial velocity in the cell middle cross-section area). A mono-phasic CFD methodology was applied for describing the rather complex bi-phasic phenomena taking place in the electrochemical oxidation of organic compounds, where gases are being formed at both electrodes. The adequacy of this assumption was subjected to validation with experimental results. Transient CFD simulations showed that the flow becomes unsteady at a rather low *Re* (in the range from 65 to 100) mainly due to the observed flow separation upstream the electrodes region. The pressure-drops determined by CFD agreed very well with the experimental measurements. Good agreement was also obtained between the Sherwood values calculated through CFD and experimentally determined by the limiting current technique. Mono-phasic CFD and experimental limiting current data were used for deriving mass-transfer correlations for the DiaCell®. These correlations were found to correctly describe *Sh* values determined from galvanostatic (electric current density of 332 A/m^2) electrochemical oxidation of selected organic compounds under mass-transfer controlled operating conditions and a turbulent-developing flow regime. These results suggest that turbulent-developing flow in an electrochemical cell can be sufficiently well described by mono-phasic CFD simulations.

1. Introduction

Electrochemical oxidation of micro-pollutants has several advantages over conventional processes. One of the most important aspects is that complete mineralisation of resilient organic micro-pollutants is usually achieved, thus making possible a large reduction in the environmental burden of polluted wastewater streams. Among the different anode electrode materials, boron-doped diamond (BDD) anodes are receiving growing attention for the removal of refractory and toxic organics from various water sources due to their large electrochemical window, non-toxicity and high resistance to corrosion, erosion and fouling. BDD anodes allow for a high efficiency for producing hydroxyl radicals from water in the electrochemical potential region of oxygen evolution according to:

$$H_2O \rightarrow {}^{\bullet}OH + H^+ + e^-$$

In commonly encountered situations, in which the concentration of organics present in water to be treated and/or the desired final organic levels are low, and under the most frequently applied galvanostatic operation conditions, the anodic oxidation of the target organic compound(s) may become mass-transfer controlled either from the very beginning or soon after the start-up of the process. However, the influence of the compound diffusivity in water on the process performance has still not been well characterized.

Enhancement of mass-transfer depends in a very important way on the disruption of the liquid boundary layers, either by introduction of physical obstacles in the flow path or by manipulation of process operating conditions, e.g. fluid flow rate. Distinct strategies have been applied to enhance mass-transfer in electrochemical flow cells, either by varying the operating conditions, or by designing new cell and electrodes geometries that aim at optimising the flow and solute distribution. Different electrochemical cell geometries used in recent years are reviewed by Jüttner et al. [1]. Among the distinct geometries, the parallel planar electrode configuration is one of the most studied for industrial applications due to its simple design, ease of manufacture, and more straightforward characterization of fluid dynamics and mass-transfer behaviour. A number of studies on mass-transfer in this type of configuration

* Corresponding author.
E-mail address: jose.santos@dq.fct.unl.pt (J.L.C. Santos).

1385-8947/$ – see front matter © 2009 Elsevier B.V. All rights reserved.
doi:10.1016/j.cej.2009.11.021

Nomenclature

A	electrode area (m^2)
C	solute molar concentration (M)
C_μ	k–ϵ turbulence model dimensionless constant = 0.09
d	channel height (m)
d_h	tube hydraulic diameter (m)
D_{AB}	mass-diffusion coefficient (m^2/s)
F	Faraday constant (C/mol)
g	gravitational constant ($m^3/(kg\,s^2)$)
I	electric current (C/s)
I_t	turbulent intensity
k	turbulent kinetic energy (m^2/s^2)
k_c	local mass-transfer coefficient (m/s)
L	average slit length (m)
L_t	turbulent length scale (m)
n	number of electrons
p	kinematic pressure (m^2/s^2)
P	atmospheric pressure (Pa)
R	universal gas constant (J/(mol K))
Re	Reynolds number, $Re = U\,d/\nu$
Sc	Schmidt number, $Sc = \nu/D_{AB}$
Sh	Sherwood number, $Sh = k_c d/D_{AB}$
$\mathbf{U}$	velocity vector (m/s)
V_{gas}	volume of gas formed (m^3)

Greek letters

ϵ	dissipation of kinetic energy (m^2/s^3)
ν	kinematic viscosity (m^2/s)
ρ	density (kg/m^3)
ω	solute mass fraction

have been made over the last decade, focusing either on entrance and exit effects, or on the effect of introducing obstacles and turbulence promoters along the flow path [2–6]. One of the most efficient electrochemical cells is the FM 01-LC electrolyser from ICI, that was studied in detail by Bengoa et al. [6]. In this work, the authors observed a significant improvement in the flow distribution by the introduction of net-type spacers and foams in the reaction region. Other promising configurations seem to be based on the impinging jet concept. The work by Polcaro et al. [7] explores such an impinging jet-based design with single inlet and outlet sections. Martínez-Huitle et al. [8] proposed a novel design in which the fluid enters the cell through a nozzle located in the center and exits through multiple peripheral outlet sections. These studies have shown that a considerable enhancement in mass-transfer is possible to be achieved in comparison to standard parallel plate designs.

One of the most often used approaches to characterize mass-transfer in electrochemical flow cells is through the limiting current technique [2–5,7–10]. This experimental procedure allows for a rigorous determination of mass-transfer coefficients with a relatively small amount of effort. It should be noted, however, that the values of mass-transfer coefficients obtained through this technique should not be directly applied for compounds having mass diffusivities which are significantly different from that of the redox couple used, usually ferri/ferrocyanide. Mass-transfer coefficients may be also determined as an adjustable fitting parameter to experimentally obtained concentration–time decay curves, if operating under mass-transfer limiting regime [7,9,11,12].

Computational fluid dynamics (CFD) is becoming a very important engineering tool for the design and simulation of process equipment [13]. The present study makes use of mono-phasic CFD to model fluid flow and mass-transfer in a frequently used electrochemical oxidation cell [11,12,14–16] with a parallel electrode configuration – DiaCell®, 106 SS/BDD from Adamant Technologies, Switzerland –, and aims at its validation with experimental measurements: pressure-drop in the flow cell, mass-transfer quantification on the anode by the limiting current technique, and mass-balance analysis of the electro-oxidation of selected organic compounds. Mass-transfer correlations are developed for the DiaCell®, based on CFD and experimental work, which may be used in place of a constant value of mass-transfer coefficient that is commonly assumed for this cell in other works. Moreover, this work also elucidates the flow patterns and Sherwood distribution in the DiaCell®. It is aimed in this study to investigate whether mono-phasic CFD modelling may be used with electro-oxidation systems, where gases are being formed at both electrodes.

2. Theory and CFD numerical method

2.1. Selected case-study

The electrochemical cell studied in this work was the DiaCell®, 106 SS/BDD from Adamant Technologies (Switzerland), assembled with a 5 mm thick polypropylene spacer (Figs. 1–3). This is a single compartment cell, in which two circular planar electrodes (a BDD anode and a stainless steel (SS) cathode) have a diameter of 9.44 cm and an area of 70 cm^2 each. An inter-electrode gap of 7 mm is provided by the spacer and two additional elastomer gaskets (1 mm thick each) that compress the spacer between the electrodes. The spacer and the gaskets comprise longitudinal segments upstream and downstream the electrodes region where the liquid flow is distributed. Due to a partial covering by the spacer, the available electrode area is reduced to 63.15 cm^2 (numerically determined in this work). The inlet circuit is formed by a cylindrical tube with a diameter of 1.5 cm, which communicates through a nozzle to a slit-type segment perpendicular to the spacer. The outlet circuit is

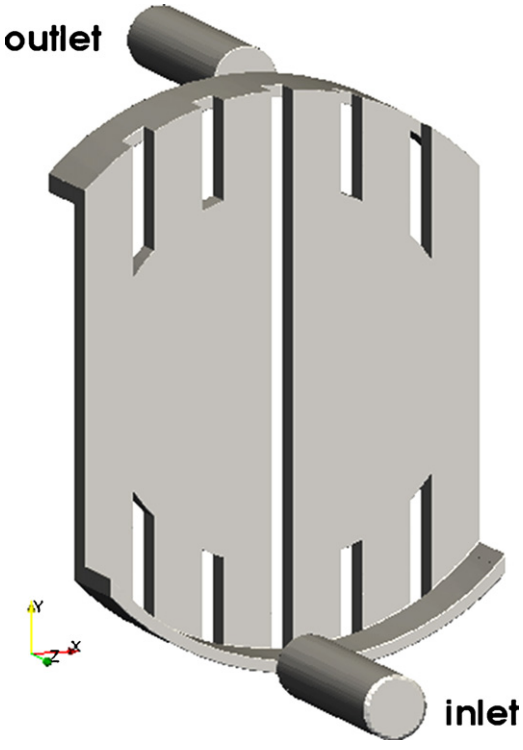

Fig. 1. Geometry of the electrochemical flow cell (DiaCell®) computational domain.

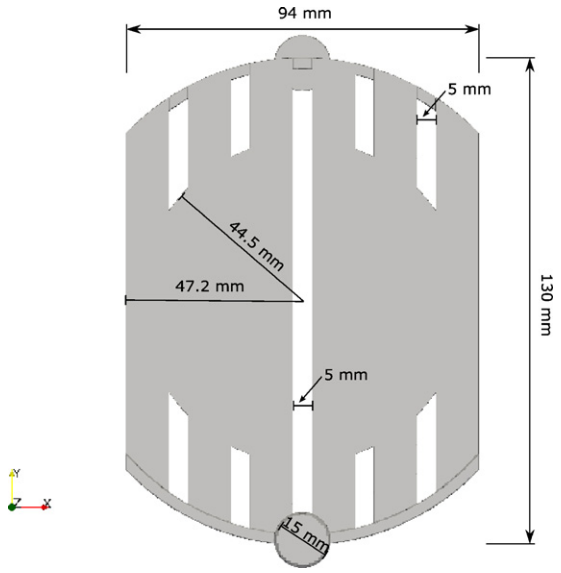

Fig. 2. Plan view of the electrochemical flow cell geometry.

equal to the inlet, where another slit-type segment communicates through a nozzle to the outlet tube.

The definition of adequate inlet profiles for velocity and turbulent quantities in the region defined by the distribution segments of the spacer depends on the knowledge about the upstream flow distribution, which is not *a priori* available. In contrast, the inlet profiles for cylindrical tubes are well studied in the literature. Due to this fact, the computational domain considered in the present study for flow and mass-transfer simulation included the entire geometry, where the inlet and outlet boundaries for simulation correspond, respectively, to the inlet and outlet cylindrical tubes.

2.2. Governing equations and boundary conditions

The governing equations of mass continuity and momentum transport for unsteady turbulent flow of an incompressible Newtonian fluid can be expressed in terms of mean flow properties and its fluctuations. The following form of the averaged equations (also known as Reynolds averaged equations) can be obtained:

$$\nabla \cdot \bar{\mathbf{U}} = 0 \tag{1}$$

$$\frac{\partial \bar{\mathbf{U}}}{\partial t} + \nabla \cdot (\overline{\mathbf{U}}\overline{\mathbf{U}}) - \nabla \cdot (\nu \nabla \bar{\mathbf{U}}) = -\nabla \bar{p} + \overline{\mathbf{U}'\mathbf{U}'} \tag{2}$$

where $\mathbf{U}$ is the fluid velocity vector, $\mathbf{U}'$ denotes its fluctuations about the mean value $\bar{\mathbf{U}}$, p is the kinematic pressure, ν is the kinematic viscosity, and $\overline{\mathbf{U}'\mathbf{U}'}$ is called the Reynolds stress tensor. In laminar flow conditions, the mean velocity and pressure in Eqs. (1) and (2) are replaced by instantaneous values, and the Reynolds stress tensor is zero, leading to a closed system of equations. Under turbulent flow conditions, the Reynolds stress tensor is a property of the flow, and additional variables need to be solved to close the system of equations. Using the Boussinesq assumption [17], the Reynolds stress tensor may be given by:

$$\overline{\mathbf{U}'\mathbf{U}'} = \nu_{\text{turb}}(\nabla \mathbf{U} + (\nabla \mathbf{U})^T) + \frac{2}{3}k\mathbf{I} \tag{3}$$

where ν_{turb} is the kinematic turbulent viscosity, $\mathbf{I}$ is the unity tensor, and k is the turbulent kinetic energy expressed by:

$$k = \frac{1}{2}\overline{\mathbf{U}' \cdot \mathbf{U}'} \tag{4}$$

The kinematic turbulent viscosity ν_{turb} is evaluated in this work as a function of the turbulent kinetic energy k and its dissipation rate ϵ using the formalism of the Launder–Sharma low-Reynolds turbulence model. For the details of the derivation of the transport equations of k and ϵ, the reader is referred to Launder and Sharma [18]. Unlike conventional turbulence models, low-Reynolds turbulence models solve the equations up to the wall, thus requiring a more refined mesh.

For an incompressible binary mixture, the solute mass fraction is governed by the solute continuity equation, given by:

$$\frac{\partial \overline{\omega_A}}{\partial t} + \nabla \cdot (\bar{\mathbf{U}}\overline{\omega_A}) - \nabla \cdot \left(\left(D_{AB} + \frac{\nu_{\text{turb}}}{Sc_{\text{turb}}} \right) \nabla \overline{\omega_A} \right) = 0 \tag{5}$$

where ω_A is the solute mass fraction, D_{AB} is its mass diffusivity, and Sc_{turb} is the turbulent Schmidt number, which is commonly considered as 0.7 for mass-transfer.

The transport equations were solved in the computational domain (see Fig. 1) assuming the following boundary conditions:

- *Inlet:* The boundary condition for velocity and turbulent variables fields was defined as a fixed average field value, where the values at the boundary are mapped from an internal plane and scaled in order to maintain the average value. In this way, the profiles of velocity and turbulent variables correspond to that of a developed flow situation. The solute mass fraction field is supplied, and the boundary condition on pressure is zero gradient.
- *Outlet:* The boundary condition for velocity, solute mass fraction and turbulent variables, is defined as zero gradient unless the flow is inward. In that case, the field value is defined as zero to prevent inflow. Pressure is defined as zero.
- *Electrodes:* The solute mass fraction on the anode is set to zero, while a zero gradient boundary condition is defined on the cathode. Velocity is set to zero and pressure is specified as zero gradient on both electrodes.
- *Walls:* For the remaining walls of the domain, a fixed value of zero is defined for velocity, and zero gradient boundary conditions are defined for both pressure and solute mass fraction.

The inlet value of the turbulent variables were defined based on a turbulent length scale $L_t = 0.07d_h$ and turbulent intensity $I_t = 0.16\,Re^{-1/8}$, where the Reynolds number is based on the tube

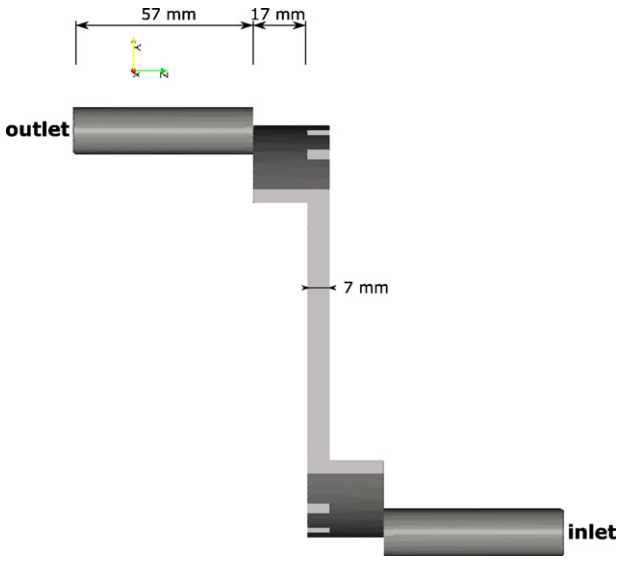

Fig. 3. Side view of the electrochemical flow cell geometry.

diameter as its characteristic dimension. The values of k and ϵ are given by:

$$k = 1.5(I_t \bar{U})^2 \quad (6)$$

$$\epsilon = \frac{C_\mu^{0.75} k^{1.5}}{L_t} \quad (7)$$

In the remaining sections of this work the Reynolds number is based on an inter-electrode distance of 7 mm as its characteristic dimension, and on a characteristic linear velocity determined as an average velocity in the transversal plane of the DiaCell®, located at $y = 6.5$ cm.

2.3. Solver development

In the present work the OpenFOAM CFD software package [19] was used for development of CFD solvers which are adequate for mass-transfer studies. OpenFOAM is based on a finite-volume approach [20] with a colocated variable arrangement. Two distinct solvers were developed: a steady-state solver and a transient solver, which were based, respectively, on simpleFoam and turbFoam (supplied with the OpenFOAM standard package). Both solvers include the transport of a solute (see Eq. (5)) and determination of mass-transfer coefficient and Sherwood number. The steady-state solver, named simpleScalarFoam, uses the SIMPLE algorithm [21] for pressure–velocity coupling, while the transient solver, turbScalarFoam, uses the PISO algorithm [21] for the same purpose. The mass-transfer coefficient is determined on the anode by assuming that the value of the solute mass fraction on the anode surface is zero:

$$k_c = \frac{D_{AB}}{\omega_{A,\text{bulk}}} \left(\frac{\delta \omega_A}{\delta z} \right) \Bigg|_{z=0} \quad (8)$$

where $\omega_{A,\text{bulk}}$ is the bulk solute mass fraction and z is the direction normal to the anode surface. The Sherwood number is then calculated by:

$$Sh = \frac{k_c d}{D_{AB}} \quad (9)$$

where d, the channel height, is the characteristic dimension of the computational domain. The source code of both simpleScalarFoam and turbScalarFoam solvers is made available at http://openfoamwiki.net for further testing and development.

2.4. Mesh generation

The computational mesh used in this work was generated using snappyHexMesh, which is supplied with OpenFOAM. The snappyHexMesh utility generates a 3D hexahedral mesh automatically from a surface mesh provided in stereolithography (STL) format. In this work, the surface mesh was generated and exported to STL format using the Salome software package [22]. The 3D meshing procedure starts with a creation of a background mesh of hexahedral cells that must include the computational domain. Then, cells which are located in the vicinity of boundary surfaces are iteratively refined and morphed in order to adjust to the surface. The last step of the meshing process introduces a pre-defined number of layers of hexahedral cells in the boundary layer.

The resulting mesh, shown in Fig. 4, yielded first-node wall distances of $y^+ < 1$ at the highest Reynolds number investigated, which is a requisite of the turbulence model used in this work. It has 1.72 million cells, and is decomposed in 15 sub-domains for parallel processing.

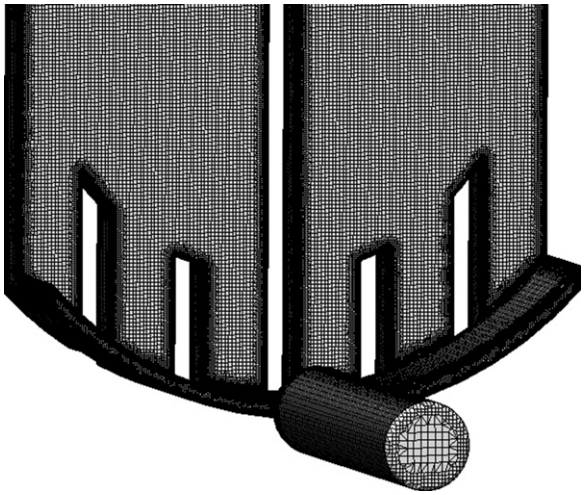

Fig. 4. The mesh used in the present work.

2.5. Discretization schemes and solution control

The convection terms in each equation were discretized in a first stage using the first-order upwind scheme until converged results were obtained. Afterwards, the convection terms in the momentum and solute mass fraction equations were discretized using the linearUpwind scheme, which is a bounded blend between the second-order central differencing scheme and the first-order upwind differencing scheme. It was decided to use the upwind scheme for the turbulent quantities due to an expected numerical instability in the solution of these equations.

The linear solvers used in this work were the algebraic multi-grid (AMG) solver for the pressure with 20 cells at the lowest multi-grid level, and the preconditioned bi-conjugate gradient (PBiCG) solver for the rest of the variables. The solver relative and absolute tolerances for the steady-state solver were set, respectively, to 0.01 and 10^{-6} for the pressure, and 0.1 and 10^{-5} for the remaining equations. Only absolute tolerances were taken into account for the transient solver, since the PISO algorithm requires full convergence on each iteration. Under-relaxation was used in the steady-state solver, with values of 0.3, 0.7, 0.5 and 0.1 for pressure, velocity, solute mass fraction, and turbulent quantities, respectively.

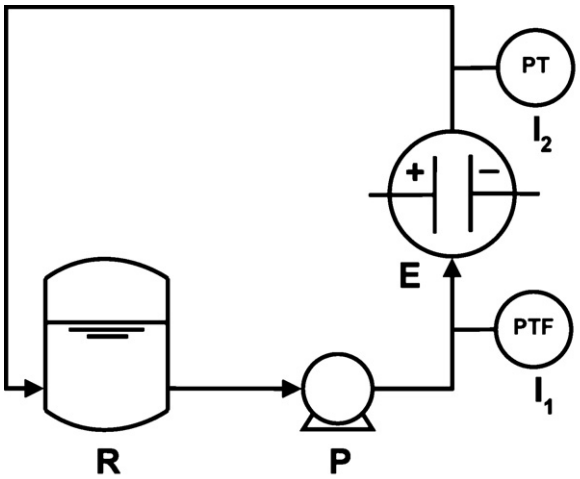

Fig. 5. Experimental set-up used in this work: R, reservoir; P, pump; E, DiaCell®; I_i, indicators (pressure, temperature and flow rate).

2.6. Simulation conditions

Simulations were processed in parallel on a 236 node AMD Opteron cluster with 2.8 GHz CPU's and 1 GB RAM/CPU. The transport properties of the fluid were defined by specifying its kinematic viscosity, $\nu = 1 \times 10^{-6}\ m^2\ s^{-1}$, and the diffusivity of the solute in water, in this case ferrocyanide, $D_{AB} = 5.62 \times 10^{-10}\ m^2\ s^{-1}$ at 18 °C. The inlet velocity was defined according to the flow rate of the pumps used in the experimental part of the work, while the solute mass fraction was set according to the solutions prepared.

The flow was solved without turbulence modelling for Reynolds values between 25 and 165, while for values above 1200, the flow was considered to be turbulent. Steady-state simulations were performed for the entire *Re* range. Transient CFD simulations were carried out at the lowest *Re* values (25–165), in order to identify the critical *Re*, which determines the transition from laminar to unsteady flow regime. The transient solver started from converged steady-state results, and was ran until obtaining a constant time-averaged mass-transfer coefficient value, usually 2 s of real simulated time. In order to guarantee temporal accuracy and numerical stability, a Courant number of less than 1 is required [21]. The Courant number, *Co*, can be defined as:

$$Co = \frac{U_0\,\delta t}{\delta x} \tag{10}$$

where δt is the time step, and δx is the cell size in the velocity direction. In order to achieve a Courant number of less than 1, the time step was set to values between 0.2 and 0.5 ms, depending on the *Re* investigated.

Steady-state CFD simulations are comparatively less expensive than transient simulations in terms of computational power, in particular in the simulation of turbulent flow, which usually require very small time-steps. In order to verify whether the results obtained in steady-state correctly describe mass-transfer in the system under study, a comparison with transient results was made at the lowest *Re* values (below 165).

The steady-state residuals for high *Re* calculations (above 1200) showed an oscillatory behaviour about a mean value, which was observed to be a result of unsteadiness of the computed flow. This unsteadiness is most probably associated with physical fluctuations in the flow, which are not fully dampen by the turbulence model and discretization schemes. This indicates that the numerical method employed in this study is not over-predicting diffusion, and that a steady-state solution is not fully achieved. In these situations, a quasi-steady solution was determined from the average of the oscillatory results.

3. Experimental

3.1. Experimental set-up

The experimental set-up, shown in Fig. 5, is comprised by the DiaCell®, described in Section 2.1, a jacketed glass feed tank, a gear pump for low *Re* with flow rate ranges of 7.5–33 L/h from Micropump, USA, or a magnetic centrifugal pump for high *Re* with a flow rate range of 390–660 L/h from ARGAL, Italy, and a rotameter to monitor the liquid flow rate. A refrigerating water thermostatic bath RE104 (Lauda Ecolin, Germany), coupled to the feed tank, was used to maintain the temperature of the feed solution at the desired set-point value.

Table 1
Transport properties of the electrolyte solution interpolated from data available in the literature [23,24].

Temperature, °C	18
Density, kg/m^3	1.03×10^{-3}
Kinematic viscosity, m^2/s	1.00×10^{-6}
Ferrocyanide diffusivity, m^2/s	5.62×10^{-10}

Table 2
Composition of the electrolyte solutions.

Reynolds number	$[KNO_3]$, M	$[K_4Fe(CN)_6]$, mM	$[K_3Fe(CN)_6]$, mM
25––165	0.5	4, 8, 12	8, 16, 24
1200––2500	0.5	0.4, 0.8, 0.12	0.8, 0.16, 0.24

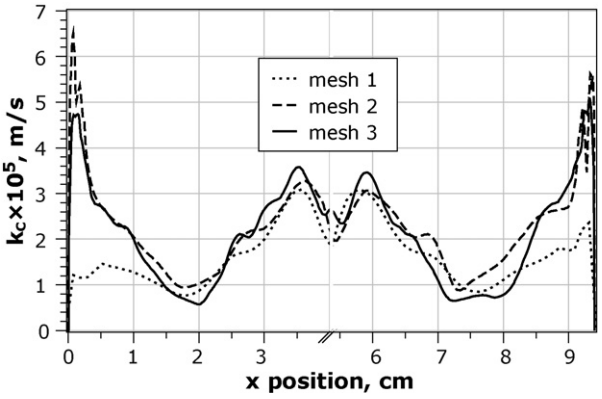

Fig. 6. Local mass-transfer coefficient values obtained for the three meshes on the anode surface, at the plane $y = 6.5$ cm for a $Re = 2500$.

For the lower flow rates, the inlet *Re*, defined with the inlet tube linear velocity and its diameter, was in the range from 190 to 1250 (inlet linear velocities ranging from 0.013 to 0.083 m/s), while the cell *Re*, based on the inter-electrode distance and on the superficial velocity in the cell middle cross-section area, ranged from 25 to 165 (linear velocities ranging from 0.0036 to 0.0236 m/s). For the higher flow rates, the inlet *Re* was in the range from 9250 to 18850 (inlet linear velocities ranging from 0.617 to 1.256 m/s). In this situation, the inlet turbulence was taken into account in the CFD simulations by an estimation of the turbulent kinetic energy and its dissipation through Eqs. (6) and (7). The corresponding cell *Re* ranged from 1200 to 2500 (cell linear velocities ranging from 0.174 to 0.355 m/s).

Table 3
Area-averaged mass-transfer coefficient on the anode surface.

	Mesh 1	Mesh 2	Mesh 3
k_c, m/s	2.26×10^{-5}	3.29×10^{-5}	3.20×10^{-5}
$\frac{k_{ci}-k_{c3}}{k_{c3}}$, %	-29.50	2.62	––

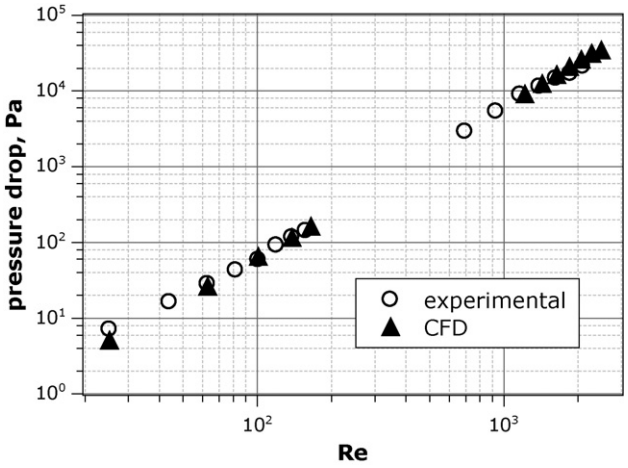

Fig. 7. Variation of pressure-drop with Reynolds number.

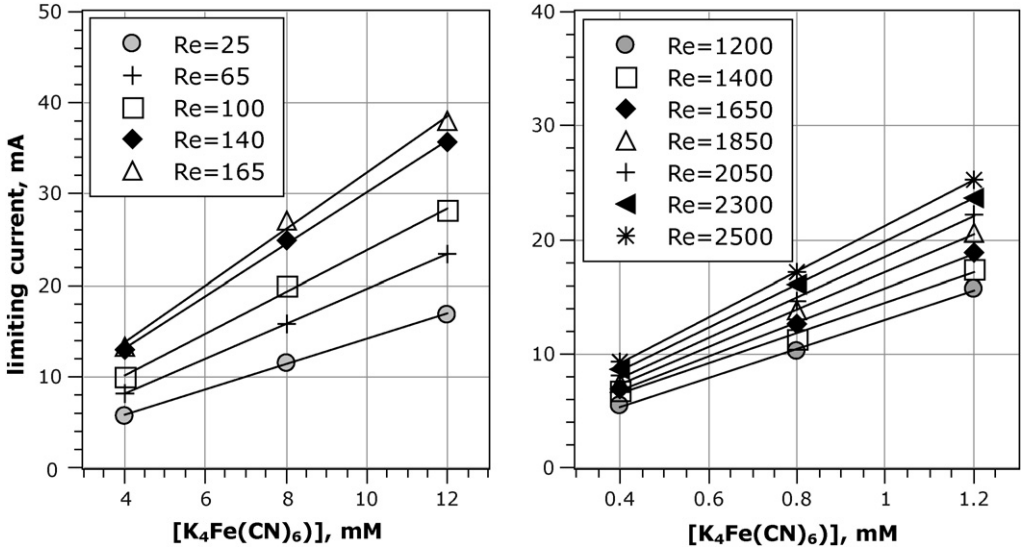

Fig. 8. Limiting current values as a function of potassium ferrocyanide concentration.

3.2. Electro-oxidation of organic compounds

Ethanol, valeric acid and propionic acid (obtained, respectively, from Panreac, Merck and Fluka) were subjected to electro-oxidation experiments performed under galvanostatic operating conditions, provided by a DiaCell-PS 500 W (Adamant Technologies, Switzerland) power supplier. Aqueous feed solutions of the individual organic compounds were prepared with a volume of 1 L, containing similar initial concentrations in the range 300–500 ppm, corresponding to 200 ppm as initial total organic carbon (TOC) content in the solutions in each case, and sodium sulphate as a supporting electrolyte with a concentration of 5 g/L.

The oxidation experiments were performed at 25 ° C and at a feed recirculation flow rate of 10 L/min ($Re = 1850$), imposing a current density of 332 A/m^2 (corresponding to a current of 2.1 A), which is well above the corresponding limiting current densities of the studied compounds in this concentration range, thus providing the desired mass-transfer controlled operation regime.

3.3. Limiting current technique for mass-transfer determination

The limiting current technique was used to determine the mass-transfer coefficients in the DiaCell®. A target ion flux to the BDD anode is a combination of electro-migration due to a potential gradient, diffusion due to a concentration gradient, and convection due to fluid flow. On the anode surface, the velocity is zero, while potential gradient contribution is negligible due to the presence of supporting electrolyte. Under such conditions, the target ion flux to the anode is solely governed by diffusion, and the area-averaged mass-transfer coefficient on the anode surface may be related to the limiting current I_{lim} by:

$$k_c = \frac{I_{lim}}{nFC_{bulk}A} \quad (11)$$

where n is the number of electrons participating in the reaction (in this case $n = 1$), F is the Faraday constant, C_{bulk} is the concentration of the oxidized ion in the bulk, and A is the area of the anode.

A BDD anode was used as the working electrode, while a stainless steel cathode was used as the counter electrode. The voltage

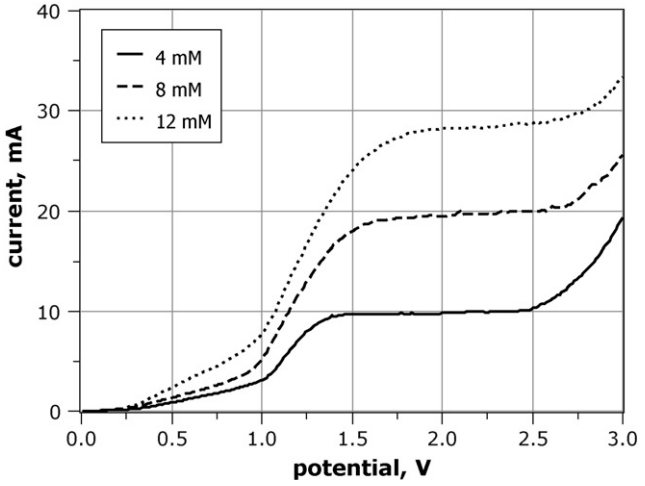

Fig. 9. Current–potential curves for $Re = 100$ and distinct $K_4Fe(CN)_6$ concentrations.

Table 4
Mass-transfer coefficient values determined by the limiting current technique and CFD.

Reynolds	$k_{c,exp} \times 10^6$ m/s	$k_{c,CFD} \times 10^6$ m/s	Error, %
25	2.28	1.86	−18.47
65	3.11	2.76	−11.16
100	3.77	3.49	−7.36
140	4.68	4.48	−4.40
165	5.07	5.17	1.89
1200	20.93	20.35	−2.79
1400	21.83	22.99	5.29
1650	24.57	26.08	6.17
1850	26.96	27.64	2.53
2050	29.06	29.37	1.05
2300	30.80	31.24	1.42
2500	32.94	32.88	−0.18

Table 5
Comparison between area-averaged mass-transfer coefficients determined for steady-state and transient CFD simulations.

Reynolds	$k_{c,transient} \times 10^6$ m/s	$k_{c,steady} \times 10^6$ m/s	Error, %
65	2.76	2.76	0.00
100	3.51	3.49	−0.57
140	4.45	4.58	2.92
165	4.91	5.17	5.29

was varied with an Autolab-10 potentiostat (Eco Chemie, Netherlands) to determine the limiting current plateaus of the polarisation curves for different flow rates and electrolyte solution concentrations focusing, on purpose, on the anodic oxidation reaction of ferrocyanide to ferricyanide.

The electrolyte solution flowing through the cell consists of a mixture of potassium ferrocyanide ($K_4Fe(CN)_6$), potassium ferricyanide ($K_3Fe(CN)_6$) and potassium nitrate (KNO_3) as a supporting electrolyte. The ferricyanide concentration was two times higher than the ferrocyanide concentration to ensure that a limiting oxidation of ferrocyanide ions occurs at the anode. Due to the limit of detection of the potentiostat used, different electrolyte concentrations were prepared for high and low *Re*. Ferrocyanide concentrations of 4, 8 and 12 mM were prepared for lower *Re* values, while for higher *Re* values the concentrations were 0.4, 0.8 and 0.12 mM, respectively. The mass-transfer coefficient was obtained through Eq. (11) by representing the limiting current in function of the ferrocyanide concentration. The transport properties of the electrolyte solution are presented in Table 1 and the different compositions are shown in Table 2. The transport properties of the electrolyte were interpolated from data available in the literature [23,24]. The solution was sparged with nitrogen for 1 h before each experimental run to remove dissolved oxygen. Nitrogen gas sparging of the solution was also maintained during the course of the experiment.

3.4. Pressure-drop determination

The pressure-drop between the inlet and the outlet of the DiaCell®, was measured at high and low Reynolds values, using an adequate pump for the flow regime under study. Pressure-drops were measured at low Reynolds values with a U-tube manometer, filled with the circulating solution and with an immiscible organic liquid, chlorobenzene, which has a density of 1102 kg/m^3 higher than the density of water. The pressure-drop Δp was then calculated by the hydrostatic equation:

$$\Delta p = \Delta y\, \Delta \rho g \tag{12}$$

where Δy is the difference in height of the organic liquid in each leg of the U-tube, $\Delta \rho$ is the difference in density of the manomet-

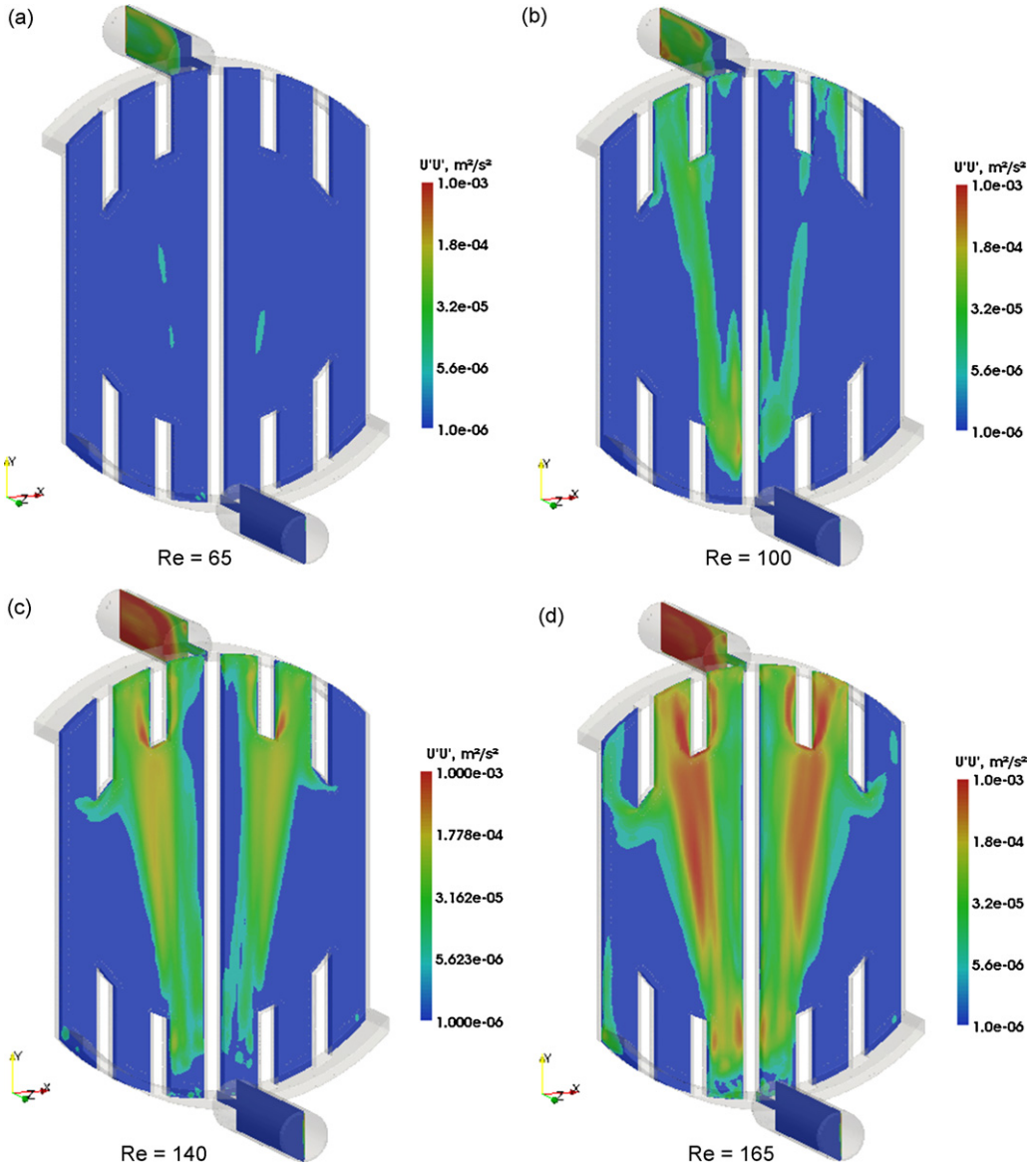

Fig. 10. Patterns of velocity fluctuations ($\mathbf{U'U'}$) at the planes $z = 3.5$ mm and $x = 0$ for $Re = 65$, 100, 140 and 165, and $Sc = 1780$: (a) $Re = 65$; (b) $Re = 100$; (c) $Re = 140$; (d) $Re = 165$.

ric fluid and water, and g is the acceleration due to gravity. For measurements at high Reynolds values, two pressure transducers (8864, Trafag, Switzerland) were mounted at the inlet and outlet of the flow cell and the pressure difference recorded.

3.5. Analytical procedures

Concentrations of propionic and valeric acids were determined by high performance liquid chromatography (HPLC) using a Merck–Hitachi apparatus equipped with a UV detector and Aminex HPX-87H column from BioRad (USA). Sulphuric acid (0.01 M) was used as the eluent at a flow rate of 0.6 mL/min and 50 ° C operating temperature. The detection wavelength was set at 210 nm. The individual organic acids concentrations were calculated through corresponding calibration curves using 10–1000 mg/L standards.

Ethanol concentrations were determined by HPLC using the same apparatus but a Merck–Hitachi differential refractometer detector (RI-71). The columns and elution conditions used were the same as referred above for organic acid determination, except for the eluent flow rate, and temperature which in this case were 0.5 mL/min and 30 °C, respectively. The ethanol concentrations were calculated through a calibration curve using 25–1000 mg/L standards.

4. Results and discussion

4.1. Grid-independence study

A grid-independence study was performed at the highest Reynolds number investigated ($Re = 2500$ based on an inter-electrode distance of 7 mm) for three meshes with an increasing number of elements: 0.63 million (mesh 1), 1.72 million (mesh 2) and 2.94 million (mesh 3). Local mass-transfer coefficient values obtained for the three meshes on the anode surface, at the plane $y = 6.5$ cm, are compared in Fig. 6, while area-averaged mass-transfer coefficient on the anode surface is compared in Table 3. The results show that the resolution of mesh 2 is capable of producing accurate results. Indeed, a visual inspection of the mass-transfer profiles in Fig. 6 shows that differences are rather small between mesh 2 and mesh 3. More importantly, an error of below 3% was

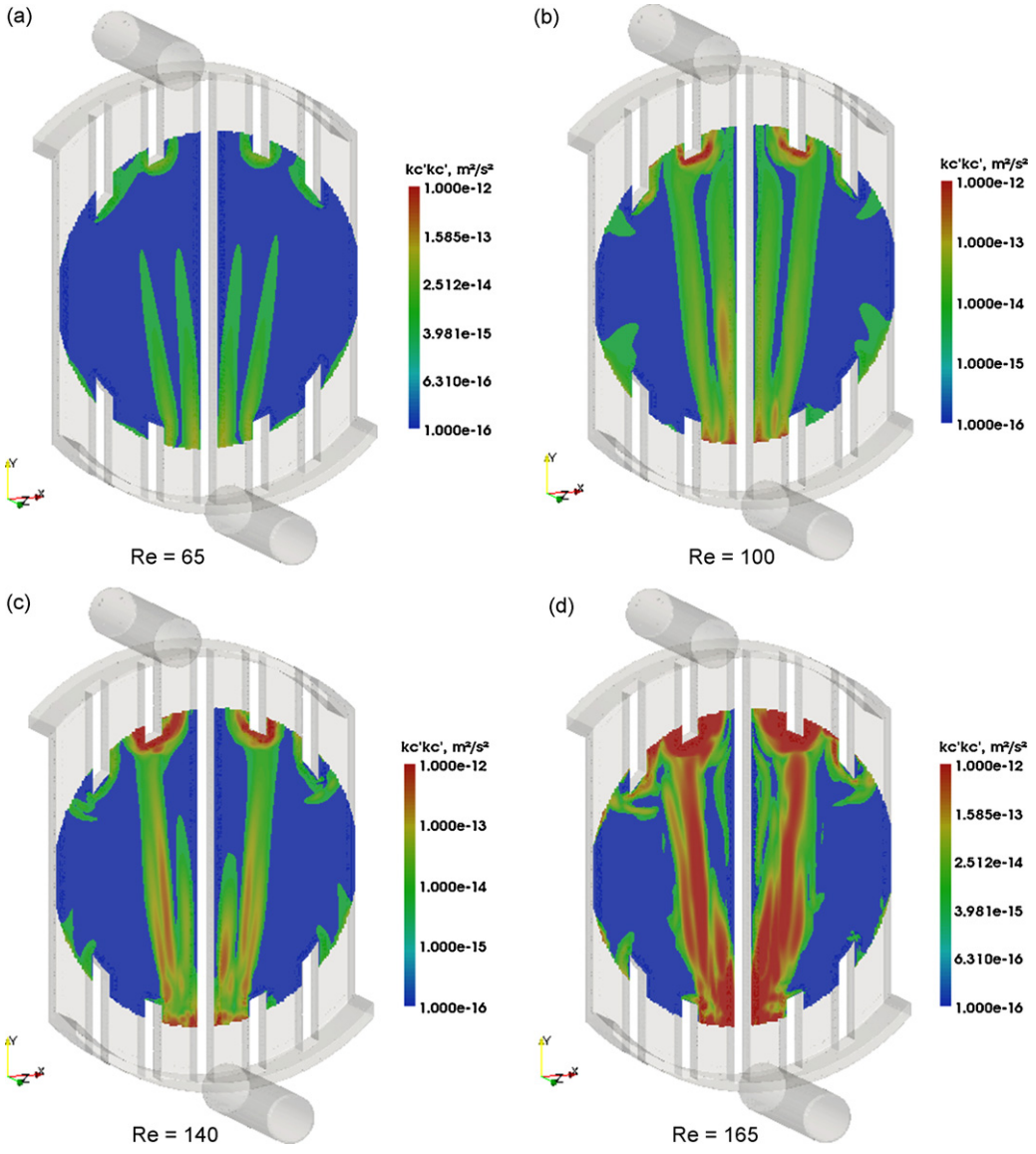

Fig. 11. Patterns of mass-transfer coefficient fluctuations ($k_c' k_c'$) on the anode for $Re = 65$, 100, 140 and 165, and $Sc = 1780$. (a) $Re = 65$; (b) $Re = 100$; (c) $Re = 140$; (d) $Re = 165$.

determined for mesh 2 for the area-averaged mass-transfer coefficient in Table 3.

4.2. Pressure-drop

A comparison between experimental and CFD pressure-drop values is shown in Fig. 7. It can be seen that the CFD predictions agree very well with the experimental results, which indicates that the computational cell geometry as well as the fluid transport properties assumptions are adequate and consistent with the experimental flow system under study. It should be mentioned that the deviation observed at the lowest *Re* is probably due to experimental error associated with measurement of such small pressure values (< 10 Pa).

4.3. Mass-transfer determination by the limiting current technique and CFD

The limiting current values obtained for the investigated Reynolds numbers are represented in Fig. 8. Fig. 9 shows typical current-potential curves used for the determination of limiting current values. The results present in Fig. 8 show a linear relation between the limiting current and ferrocyanide concentration for all the experiments, which justifies the use of Eq. (11) for calculating mass-transfer coefficients. The mass-transfer coefficient values obtained by the limiting current technique are listed in Table 4 along with those obtained by CFD. The error of CFD calculations is typically lower than 8%, although being larger at the lowest *Re*. The reason for the larger deviation observed at the lowest *Re* is discussed in Section 4.5.

4.4. Velocity and mass-transfer patterns determined by CFD

The results from transient CFD simulations are depicted in Figs. 10 and 11, where it can be seen that important fluctuations in velocity ($\mathbf{U}'\mathbf{U}'$) and mass-transfer coefficient ($k_c'k_c'$) fields at the planes $z = 3.5$ mm and $x = 0$ start to occur for a $Re = 100$, which indicates that the critical *Re* for the DiaCell®, is in the range from 65 to 100. With increasing *Re*, the oscillatory behaviour of the flow becomes more evident, in particular in the vicinity of the longitu-

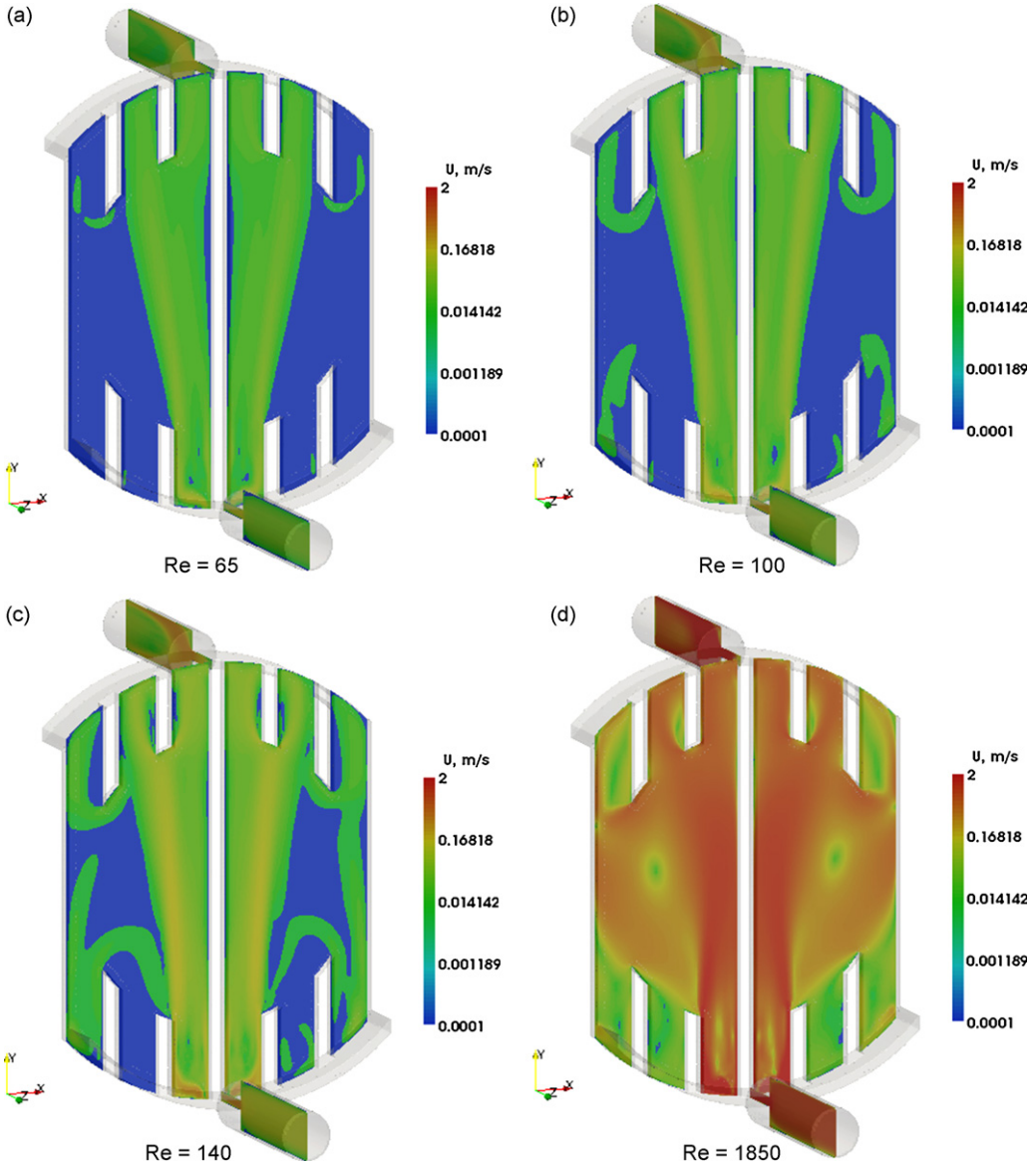

Fig. 12. Patterns of velocity magnitude at the planes $z = 3.5$ mm and $x = 0$ for $Re = 65$, 100, 140 and 1850, and $Sc = 1780$. (a) $Re = 65$; (b) $Re = 100$; (c) $Re = 140$; (d) $Re = 1850$.

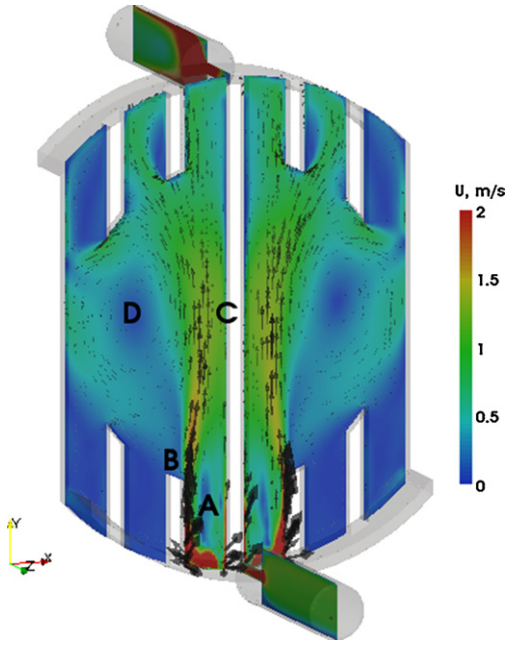

Fig. 13. Patterns and vectors of velocity magnitude at the planes $z = 3.5$ mm and $x = 0$ for $Re = 1850$ and $Sc = 1780$.

dinal central spacer walls. For *Re* below 100, the flow is laminar in most regions except in the outlet cylindrical tube, where instabilities are generated downstream the nozzle.

Table 5 shows a comparison between area-averaged mass-transfer coefficients determined for steady-state and transient CFD simulations. It can be seen that the steady-state mass-transfer coefficients compare very well with those obtained with transient CFD. Therefore, it may be assumed that steady-state results accurately estimate mass-transfer on the anode of the DiaCell®. Due to this fact, the numerical results shown in the subsequent sections of this work are based on steady-state CFD.

Fig. 12 shows the velocity magnitude pattern at the planes $z = 3.5$ mm and $x = 0$ for *Re* values representative of distinct flow regimes: laminar (65), critical (100), unsteady-laminar (140) and turbulent-developing (1850). The main features of the fluid flow are similar for all *Re* values, being clear that developed flows were not obtained for the range of *Re* studied. The turbulent-developing *Re* value of 1850 meets the mass flow rate specifications indicated by the manufacturer of the DiaCell®, therefore its flow patterns are analysed in detail in Fig. 13. It may be seen that the flow is distributed in a symmetric way in relation to the $x = 0$ plane. The fluid accelerates in the nozzle that connects the inlet tube to the slit-type section, thus forming an impinging jet that directs the flow mainly to the two central segments upstream the electrodes region. In those central segments, recirculation zones are observed (region A in Fig. 13), which are smoothed out when the fluid enters the electrodes region. Due to the design of the feed section, the remaining inlet flow distribution segments show a comparatively lower velocity magnitude. The flow profile in the electrodes region is greatly affected by the upstream flow distribution, being mainly driven close to the central longitudinal spacer walls through a jetting effect. Other important features are the observed flow separation at the corner of the inlet central distribution segments (region B in Fig. 13), and its reattachment to the central spacer walls at the center of the domain (region C in Fig. 13). Large recirculation zones (region D in Fig. 13) develop from the central longitudinal spacer walls back to the inlet distribution segments, creating low velocity regions close to the center of the domain. In the downstream region the flow is again mainly converged to the center segments of the distribution circuit.

It becomes clear that the Sherwood field patterns on the anode surface for the same *Re* values as before, shown in Fig. 14, result in a very important way from the wall shear stress patterns observed in Fig. 15. Regions of enhanced mass-transfer are located in the vicinity of the central spacer walls and near the central outlet distribution segments, where a more important effect of wall shear stress is observed. In contrast, the mass-transfer efficiency is lower in the remaining sections of the anode. Mass-transfer efficiency on the anode expressed in the form of histograms for each *Re* value (see Fig. 16) reinforces these observations by disclosing a non-uniform distribution of Sherwood number over the anode area, where regions of lower mass-transfer efficiency are dominant. These results show that the situation is far from the optimal one, in which a uniform *Sh* distribution would be envisaged. It is interesting to note that a change in the flow regime does not greatly affect the *Sh* distribution over the anode. Nevertheless, the *Sh* distribution for $Re = 1850$, representative for a turbulent-developing flow regime, is comparatively better than that at the other *Re* values. It is also observed that the onset of unsteady flow at $Re = 100$ has a negative effect on the *Sh* distribution compared to $Re = 65$. This was observed to be a result of augmented local *Sh* values due to unsteadiness that builds up in the vicinity of the corner of the inlet central distribution segments.

It is then evident that the flow distribution in the DiaCell®, is not optimal, and consequently its mass-transfer performance is clearly inferior to other electrochemical cell configurations, such as, for example, those studied by Bengoa et al. [6], Polcaro et al. [7] and Martínez-Huitle et al. [8]. These works suggest distinct strategies that may be followed for improving the DiaCell®, mass-transfer performance either by re-designing its inlet and outlet circuits or by introducing turbulence promoters in the reaction region.

4.5. Mass-transfer correlations

The values of mass-transfer coefficients obtained by the limiting current technique and by CFD were used to obtain mass-transfer correlations in the form:

$$Sh = a\,Re^{b}Sc^{1/3} \tag{13}$$

where *a* and *b* are fitting parameters. Fig. 17 shows $Sh/Sc^{1/3}$ values plotted against *Re* values for the limiting current technique and CFD work. The correlations determined in this work are listed in Table 6, grouped by their adequacy for laminar of turbulent-developing flow regime.

The experimental and CFD results show a very good agreement except for a slight deviation in the lower *Re* range, where the experimental values are larger than CFD values. This may result from the vertical orientation of the DiaCell®, in the experimental set-up, which can lead to a natural convection effect due to concentration gradients, that was not taken into account in CFD simulations.

Table 6
Mass-transfer correlations determined by the experimental limiting current technique and CFD.

	Correlation	Reynolds range
Experimental	$Sh = 0.689Re^{0.36}\,Sc^{1/3}$	$25 < Re < 100$
CFD	$Sh = 0.417Re^{0.45}\,Sc^{1/3}$	$25 < Re < 100$
Experimental	$Sh = 0.141Re^{0.70}\,Sc^{1/3}$	$100 < Re < 2500$
CFD	$Sh = 0.123Re^{0.72}\,Sc^{1/3}$	$100 < Re < 2500$

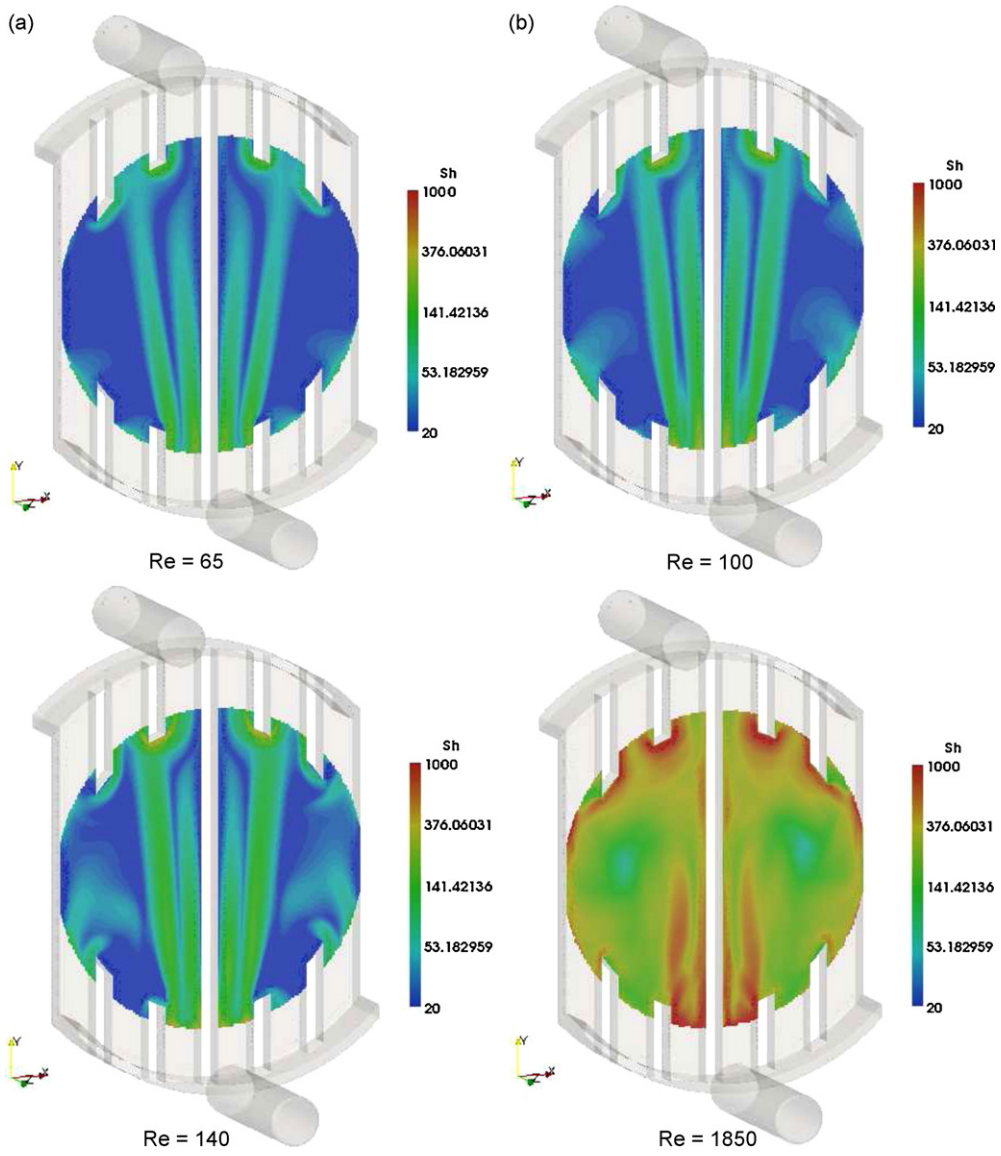

Fig. 14. Patterns of Sherwood on the anode for $Re = 65$, 100, 140 and 1850, and $Sc = 1780$. (a) $Re = 65$; (b) $Re = 100$; (c) $Re = 140$; (d) $Re = 1850$

An important aspect observed in Fig. 17 is that the critical Reynolds number for the DiaCell®, which determines the transition from laminar to unsteady flow regime, appears to occur for *Re* in the range from 65 to 100, which is considerably lower than the critical value for a rectangular slit, which usually begins at about $Re = 1000$ [17]. The onset of unsteady flow regime for $Re = 100$ was also observed in the transient CFD results presented in Section 4.4. The transition in flow regime at such a low *Re* value was observed to be a result of the flow separation at the corners of the inlet flow distribution segments (see Figs. 10 and 12) which inducted an oscillatory behaviour of the flow in that region.

4.6. Electro-oxidation of organic compounds

The electro-oxidation data of ethanol, valeric acid and propionic acid were fitted with the following batch mass-balance equation:

$$\ln\left(\frac{C_{org}}{C_{org,0}}\right) = -\frac{k_c A}{V}t \quad (14)$$

where C_{org} is the concentration of the organic compound at time t, $C_{org,0}$ is its initial concentration, A is the area of the anode, V is the volume of the feed solution, and t is the time.

The concentration decays of the studied organic compounds are presented in Fig. 18. As it can be observed, they fit well with a pseudo-first-order kinetic pattern that is characteristic for a mass-transfer controlled operation. The latter justifies the use of Eq. (14) and indicates that k_c in this equation actually represents the average mass-transfer coefficient of the target compound over the electrochemical cell and the reservoir under the tested conditions of relatively high current density and low compound concentrations. Under such conditions, only a fraction of the applied current, equal to the limiting current, is used for the oxidation of the target compound while the rest is used for side reactions, mainly represented by oxygen evolution [25].

$Sh/Sc^{1/3}$ values obtained from Eq. (14) are compared in Table 7 to values predicted with the correlations determined in this work. The deviation of the $Sh/Sc^{1/3}$ values determined from Eq. (14), and presented in the last columns of Table 7, is lower than 18% when compared to values predicted using the correlations from this work. While a local increase in mass-transfer would be gener-

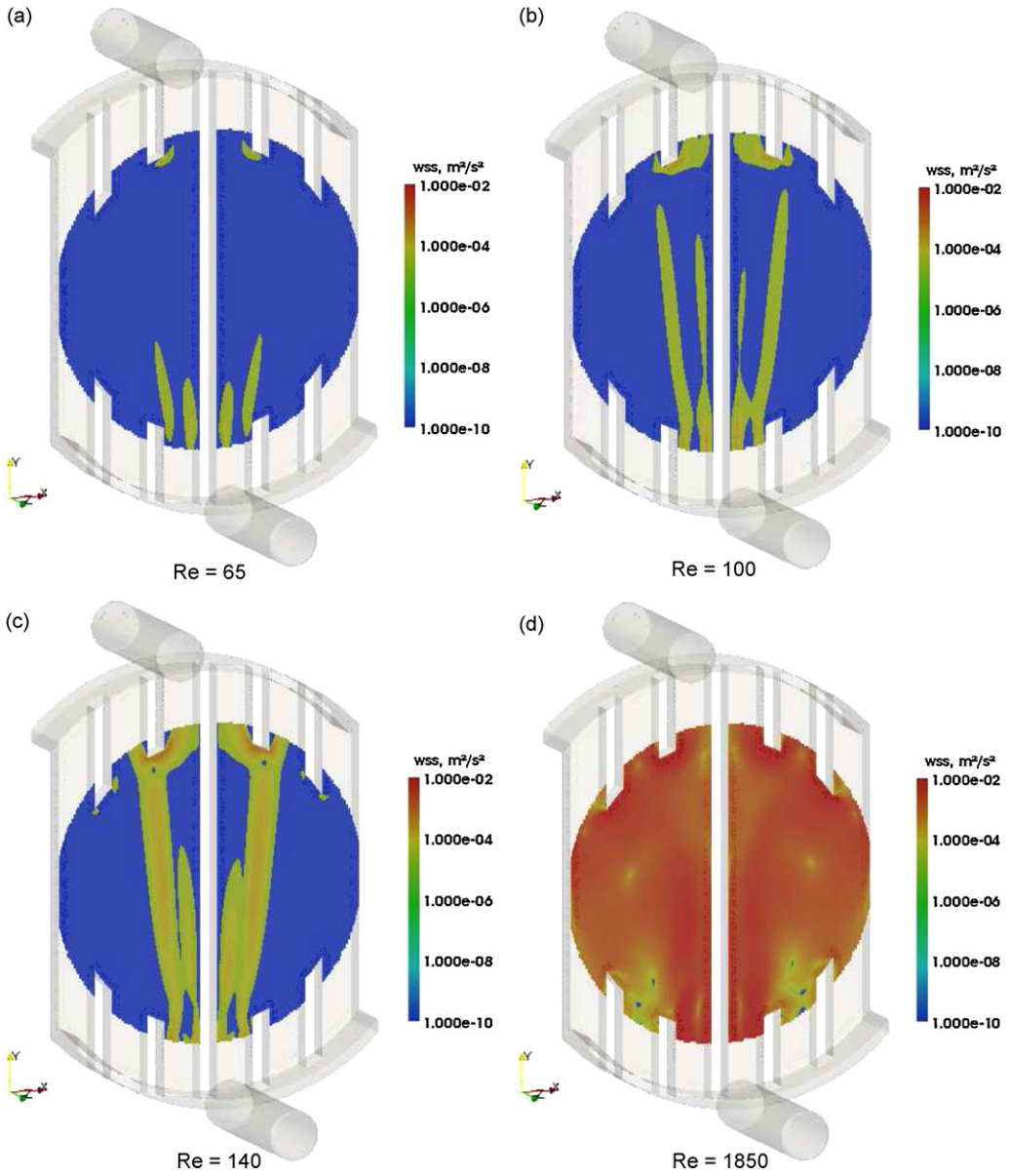

Fig. 15. Patterns of wall shear stress on the anode for $Re = 65$, 100, 140 and 1850, and $Sc = 1780$. (a) $Re = 65$; (b) $Re = 100$; (c) $Re = 140$; (d) $Re = 1850$.

ally expected to occur if gas bubbles were formed at the working electrode, the results show an opposite tendency. Such a behaviour might be possibly attributed to a partial adsorption of the studied organic compounds on the BDD electrode surface [26]. If the electrode surface were partially covered by organics, this could result in displacement of water from the surface and, as a consequence, the rate of water discharge would be also reduced. Under such conditions, the mass-transfer coefficients obtained through Eq. (14) might have lumped some reaction-associated effects.

If it is considered that all the current applied is used for electrolysis of water and there are no side reactions, 4 mol of electrons must produce 2 mol of H_2 gas and 1 mol of O_2 gas. Thus, the theoretical (maximum) volume of hydrogen and oxygen produced V_{gas}, can be deduced from the data for current and time, following Faraday's first law of electrolysis as:

$$V_{gas} = \frac{IRTt}{nFP} \quad (15)$$

where $R = 8.314\,J/(mol\,K)$ is the universal gas constant, I is the current applied in Coulombs per second, T is the working temperature in K, t is the time in seconds, $F = 96485$ is the Faraday's constant in Coulombs per mol, $P = 1 \times 10^5$ Pa is the atmospheric pressure, n is number of electrons = 2 for H_2, and 4 for O_2, respectively. For the applied current of 2.1 A and at the working solution temperature of 298 K, this would result in an overall gas production of about 1.46 L/h (composed by 0.970 L/h of H_2 and 0.485 L/h of O_2). Considering a liquid flow rate of 600 L/h, the corresponding gas hold-up is determined as 0.24%. It might be expected that such conditions are well approximated, especially at the end of the mineralization of the organic compounds studied. This simple calculation indicates that the formation of gases in the DiaCell®, under the tested conditions is not significant in terms of overall gas hold-up. Local gas hold-up values in the vicinity of the electrodes may be clearly superior, leading to a bi-phasic flow situation in these regions; however, even under such conditions, the results present in Table 7 demonstrate that mono-phasic CFD simulations are adequate and may be used with

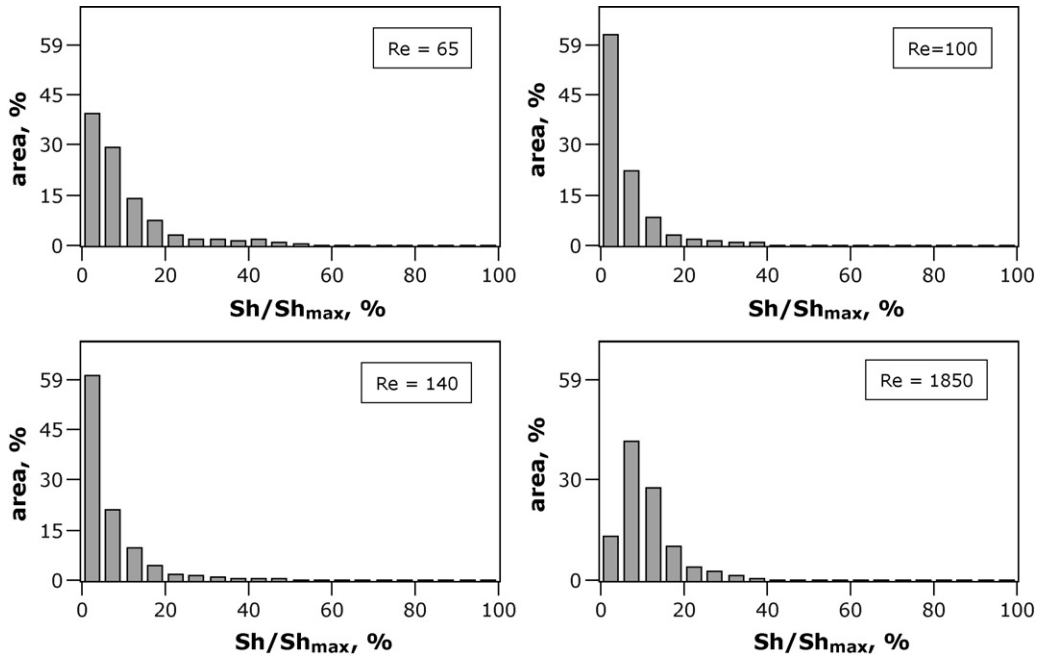

Fig. 16. Histograms of percentage area as a function of Sh/Sh_{max} for $Re = 65$, 100, 140 and 1850, and $Sc = 1780$.

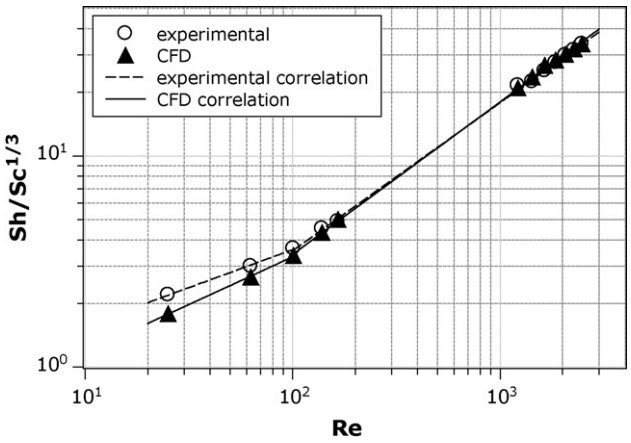

Fig. 17. Plot of $Sh/Sc^{1/3}$ against Re for the limiting current technique and CFD.

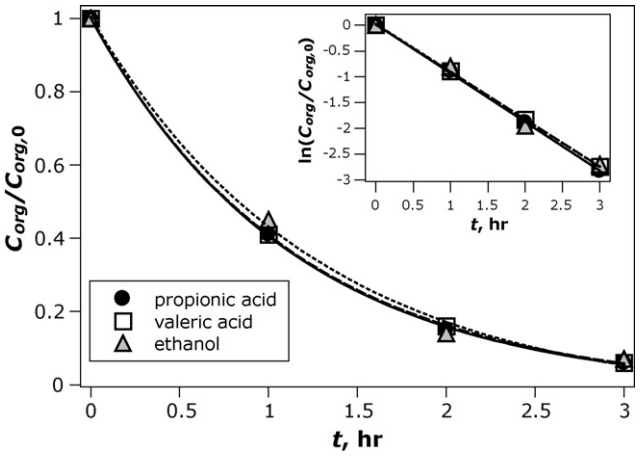

Fig. 18. Concentration decays with time of propionic and valeric acids, and ethanol. The inset figure shows a semi-logarithmic representation of concentration decays.

Table 7
Comparison between $Sh/Sc^{1/3}$ determined from the electro-oxidation of target organic compounds with predictions using CFD and experimental mass-transfer correlations for $Re = 1850$. The diffusivity values were taken from Schramke et al. [27].

	$D_{AB}^{25\,^\circ C} \times 10^9$, m^2/s	Sc	$Sh_{org}/Sc^{1/3}$	$Error_{CFD}$, %	$Error_{exp}$, %
Propionic acid	1.10	811.82	28.40	−7.09	−5.00
Valeric acid	1.20	744.17	25.97	−15.05	−13.14
Ethanol	1.27	703.15	25.17	−17.66	−15.81

confidence.

Moreover, the applied current densities are clearly above the limiting electric current density of the organic compounds. Under such conditions, due to the distinct ion diffusivities of the supporting salt electrolyte, departures from local electroneutrality are expected to occur, which can lead to electro-convection effects very near the anode [17]. However, such effects appear to be also neglible at this Re value.

5. Conclusions

It has been shown that a combination of mono-phasic CFD, limiting current technique and pressure-drop measurements is useful for understanding flow and mass-transfer phenomena in the investigated electrochemical oxidation cell. In particular, the 3D flow structure and the Sh distribution over the DiaCell®, anode was possible to be determined by CFD simulations. It was found by transient CFD simulations that instabilities in the flow start to occur for a relatively low Re in the range from 65 to 100, which can be assumed as the critical Re range for the DiaCell®, above which a change in the flow regime and a positive shift in the mass-transfer dependence on Re is observed. The results obtained for the laminar flow region can be useful for example in the processing of highly viscous solutions.

As steady-state CFD simulations provided accurate results when compared to transient ones, they were used to develop mass-transfer correlations in both laminar and unsteady flow regime: $Sh = 0.417Re^{0.45}\,Sc^{1/3}$ and $Sh = 0.123Re^{0.72}\,Sc^{1/3}$, respec-

tively. Moreover, experimental results obtained with the limiting current technique were also compiled in the form of mass-transfer correlations: $Sh = 0.689Re^{0.36}\,Sc^{1/3}$ and $Sh = 0.141Re^{0.70}\,Sc^{1/3}$. As can be seen, the correlations obtained through these distinct approaches agree very well, in particular for unsteady flow regime. These correlations were found to agree well also with the *Sh* values obtained by curve-fitting of the concentration decays of the investigated organic compounds under mass-transfer controlled operating conditions. It was found out that turbulent-developing flow in the studied electrochemical cell can be adequately described by mono-phasic CFD simulations, which significantly simplifies its mass-transfer characterization and can serve as a valuable tool for its optimization.

The results show that valuable engineering data can be obtained using the methodology described in this work. Its extension to other electrochemical flow cells is expected to be straightforward.

References

[1] K. Jüttner, U. Galla, H. Schmieder, Electrochemical approaches to environmental problems in the process industry, Electrochimica Acta 45 (15–16) (2000) 2575–2594.

[2] C.F. Oduoza, A.A. Wragg, Local mass-transfer distribution in the channels of a serpentine flow baffled parallel plate cell, Chemical Engineering Journal 85 (2–3) (2002) 119–126.

[3] A. Djati, M. Brahimi, J. Legrand, B. Saidani, Entrance effect on mass transfer in a parallel plate electrochemical reactor, Journal of Applied Electrochemistry 31 (8) (2001) 833–837.

[4] C. Oduoza, A. Wragg, M. Patrick, The effects of a variety of wall obstructions on local mass transfer in a parallel plate electrochemical flow cell, Chemical Engineering Journal 68 (2–3) (1997) 145–155.

[5] A. Wragg, A. Leontaritis, Local mass transfer and current distribution in baffled and unbaffled parallel plate electrochemical reactors, Chemical Engineering Journal 66 (1) (1997) 1–10.

[6] C. Bengoa, A. Montillet, P. Legentilhomme, J. Legrand, Characterization and modeling of the hydrodynamic behavior in the filter-press-type FM01-LC electrochemical cell by direct flow visualization and residence time distribution, Industrial and Engineering Chemistry Research 39 (7) (2000) 2199–2206.

[7] A. Polcaro, A. Vacca, S. Palmas, M. Mascia, Electrochemical treatment of wastewater containing phenolic compounds: oxidation at boron-doped diamond electrodes, Journal of Applied Electrochemistry 33 (10) (2003) 885–892.

[8] C.A. Martínez-Huitle, S. Ferro, A. De Battisti, Electrochemical incineration of oxalic acid: reactivity and engineering parameters, Journal of Applied Electrochemistry 35 (11) (2005) 1087–1093.

[9] A. Liao, M. Spitzer, A. Motheo, R. Bertazzoli, Electrocombustion of humic acid and removal of algae from aqueous solutions, Journal of Applied Electrochemistry 38 (5) (2008) 721–727.

[10] P. Canizares, J. Garcia-Gomez, J. Lobato, M. Rodrigo, Modeling of wastewater electro-oxidation processes. Part I. general description and application to inactive electrodes, Industrial and Engineering Chemistry Research 43 (9) (2004) 1915–1922.

[11] E. Weiss, K. Groenen-Serrano, A. Savall, A comparison of electrochemical degradation of phenol on boron doped diamond and lead dioxide anodes, Journal of Applied Electrochemistry 38 (3) (2008) 329–337.

[12] A. Cabeza, A.M. Urtiaga, I. Ortiz, Electrochemical treatment of landfill leachates using a boron-doped diamond anode, Industrial and Engineering Chemistry Research 46 (5) (2007) 1439–1446.

[13] J. Joshi, V. Ranade, Computational fluid dynamics for designing process equipment: expectations, current status, and path forward, Industrial and Engineering Chemistry Research 42 (6) (2003) 1115–1128.

[14] C. Flox, C. Arias, E. Brillas, A. Savall, K. Groenen-Serrano, Electrochemical incineration of cresols: A comparative study between PbO_2 and boron-doped diamond anodes, Chemosphere 74 (2008) 1340–1347.

[15] A. Urtiaga, A. Rueda, A. Anglada, I. Ortiz, Integrated treatment of landfill leachates including electrooxidation at pilot plant scale, Journal of Hazardous Materials 166 (2009) 1530–1534.

[16] A. Anglada, A. Urtiaga, I. Ortiz, Pilot scale performance of the electro-oxidation of landfill leachate at boron-doped diamond anodes, Environmental Science and Technology 43 (6) (2009) 2035–2040.

[17] R. Byron Bird, W. Stewart, E. Lightfoot, Transport Phenomena, Wiley, 2002.

[18] B. Launder, B. Sharma, Application of the energy-dissipation model of turbulence to the calculation of flow near a spinning disc, Letters in Heat and Mass Transfer 1 (2) (1974) 131–138.

[19] OpenCFD Ltd, OpenFOAM: The Open Source CFD Toolbox. http://www.opencfd.co.uk/openfoam/.

[20] S. Patankar, Numerical Heat Transfer and Fluid Flow, Taylor & Francis, 1980.

[21] J. Ferziger, M. Perić, Computational Methods for Fluid Dynamics, Springer, New York, 1999.

[22] Open Cascade SAS (OCC), Salome. http://www.salome-platform.org.

[23] C. Lin, E. Denton, H. Gaskill, G. Putnam, Diffusion-controlled electrode reactions, Industrial and Engineering Chemistry Research 43 (9) (1951) 2136–2143.

[24] T. Isono, Density, viscosity, and electrolytic conductivity of concentrated aqueous electrolyte solutions at several temperatures, Journal of Chemical and Engineering Data 29 (1984) 45–52.

[25] A. Kapalka, G. Fóti, C. Comninellis, Kinetic modelling of the electrochemical mineralization of organic pollutants for wastewater treatment, Journal of Applied Electrochemistry 38 (1) (2008) 7–16.

[26] A. Kapalka, G. Fóti, C. Comninellis, Investigation of the anodic oxidation of acetic acid on boron-doped diamond electrodes, Journal of the Electrochemical Society 155 (3) (2008) E27–E32.

[27] J. Schramke, S. Murphy, W. Doucette, W. Hintze, Prediction of aqueous diffusion coefficients for organic compounds at 25 °C, Chemosphere 38 (10) (1999) 2381–2406.